AMBISONICS SYMPOSIUM 2011
June 2-3, Lexington, KY

DERIVATION OF AMBISONICS SIGNALS AND PLANE WAVE DESCRIPTION OF MEASURED SOUND FIELD USING IRREGULAR MICROPHONE ARRAYS AND INVERSE PROBLEM THEORY

P.-A. Gauthier[1], É. Chambatte[1], C. Camier[1], Y. Pasco[1], A. Berry[1]

[1] Groupe d'Acoustique de l'Université de Sherbrooke,
2500 boul. de l'Université, Sherbrooke, Québec, J1K 2R1 CANADA
Philippe-Aubert.Gauthier@USherbrooke.ca

Abstract: *Spatial sound field reproduction involves two steps: spatial sound field capture and subsequent spatial sound field reproduction. This paper deals with sound field capture within the context of aircraft cabin sound environment reproduction while complying to practical and geometrical constraints. Higher-order Ambisonics (HOA) are common tools for spatial sound capture. Spherical microphone arrays are often used for this purpose. However, in some practical situations, one may favor irregular or non-spherical array geometry. This is the purpose of this paper. Sound field extrapolation (SFE) is aimed at the prediction of a sound field in an extrapolation region using a microphone array in a measurement region different from the extrapolation region. The reported SFE method is based on an inverse problem formulation combined with a recently proposed regularization method: a beamforming matrix in the discrete smoothing norm of the cost function. In post-processing stages, we are interested in the derivation of HOA signals from the inverse problem solution. The HOA signals are derived from the plane wave amplitudes obtained by the resolution of the inverse problem. This approach gives the B-Format Ambisonics signals at each point of the extrapolation region, thus providing a virtually movable Ambisonic microphone. Experimental results which validate the proposed SFE method in an extrapolation region are presented. The paper finally presents the predicted Ambisonics signals from the SFE method applied to the experimental SFE.*

Key words: Ambisonics, higher-order Ambisonics, microphone array, sound field extrapolation, beamforming, inverse problem, virtual acoustics, virtual Ambisonics microphones

1 INTRODUCTION

Spatial sound field reproduction usually involves two steps: spatial sound field capture and subsequent spatial sound field reproduction [1]. Metrics derived from the captured sound field (sound pressure level, sound energy density, source localization, etc.) will depend on the experimental technique employed in the sound field capture. Usually, sound fields are measured in areas such as outdoor places, concert halls [2], or more confined spaces such as vehicle interiors. This paper deals with microphone array processing within the context of aircraft cabin sound environment reproduction [3, 4].

In many situations, the spatial sound capture phase raises the specific problem of choosing the measurement technique which will provide the more extended and accurate sound field measurement while complying to practical constraints. Ambisonics-based systems and higher-order Ambisonics (HOA) are common tools for this kind of problem [5]. Through a spherical harmonic decomposition of the local sound pressure field, they have the ability to provide sound pressure levels and directions of propagation with a low number of transmitted channels. The main drawback is that the sound field information is local and extrapolation of the sound field to other locations is difficult, implying the need to multiply the number of measurement positions or to increase the Ambisonics order. Spherical microphone arrays are often used for this purpose. However, in some practical situations, one may favor irregular or non-spherical array geometry [1]. This paper considers irregular array geometry.

For spatial sound field reproduction purpose, one is typically interested by the use of microphone arrays in order to extrapolate the sound field outside the measurement region. In general, sound field extrapolation (SFE) is aimed at the prediction of a sound field in an extrapolation region using a microphone array in a measurement region different from the extrapolation region [6]. SFE finds application in noise source identification, sound source localization [7], sound source reconstruction [6, 8, 9] and sound field measurement for spatial audio [2, 10]. In the context of sound field reproduction in a vehicle cabin, we are interested in the derivation of first-order (B-format) and HOA signals from an arbitrary and irregular microphone array. The derivation of Ambisonics signals from an irregular array geometry should be based on a method that circumvents the fact that the spheri-

cal harmonics are not necessarily orthogonal functions over the spatially-sampled region defined by an irregular or arbitrary microphone array geometry [1]. To circumvent this, we recently proposed a method based on sound field extrapolation that combines inverse problem theory and beamforming [11].

This method is based on an inverse problem formulation combined with a recently proposed regularization approach: a beamforming matrix in the discrete smoothing norm of the cost function. In our application, the inverse solution is a set of plane waves that best approximates the sound field captured by the array. The B-Format Ambisonics first-order signals W, X, Y and Z are finally derived from the plane wave complex amplitudes obtained by the resolution of the discrete inverse problem. This approach gives the B-Format Ambisonics signals at each point of the extrapolation region, thus providing a virtually movable Ambisonics microphone. Furthermore, the derivation of HOA signals is possible.

This paper presents the derivation of the HOA signals from the SFE results along with the first experimental validation of the proposed SFE method based on the beamforming regularization matrix.

1.1. Paper structure

Section 2 recalls the recently developed SFE method based on inverse problem theory and beamforming regularization matrix. The derivation of the HOA signals from the SFE solution is presented in Sec. 3.1. Numerical results to verify the HOA signals derivation method are presented in Sec. 3.2. The experiments and corresponding results are described in Sec. 4. To facilitate the understanding of the potential applications of the proposed approach, Sec. 5 illustrates a possible implementation of the proposed method. A short conclusion closes the paper. Full-page figures are presented at the end of the paper.

2 INVERSE PROBLEMS: THEORY

The generic microphone array and coordinate system are shown in Fig. 1. The array includes M microphones. For a given frequency, a complex sound pressure field measurement is stored in $\hat{\mathbf{p}}(\mathbf{x}_m) \in \mathbb{C}^M$. In this paper, bold small letters represent vectors and capital bold letters represent matrices.

2.1. Inverse problem: Tikhonov regularization

The general discrete direct sound radiation problem in matrix form is:

$$\mathbf{p}(\mathbf{x}_m) = \mathbf{G}(\mathbf{x}_m, \mathbf{y}_l)\mathbf{q}(\mathbf{y}_l), \tag{1}$$

with

$$\mathbf{p} \in \mathbb{C}^M, \mathbf{G} \in \mathbb{C}^{M\times L} \text{ and } \mathbf{q} \in \mathbb{C}^L, \tag{2}$$

where $\mathbf{q}$ is the monopolar source strength [12] vector, $\mathbf{G}$ is the transfer matrix that represents sound radiation and $\mathbf{p}$ is the resulting sound pressure vector at the microphone locations $\mathbf{x}_m$. The l-th source is located in $\mathbf{y}_l$. In this paper,

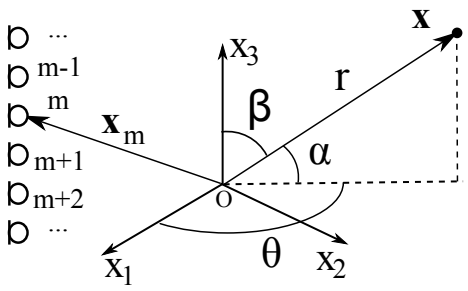

Figure 1: Illustration of the spherical and rectangular coordinate systems. Microphones are located in $\mathbf{x}_m$. Any field point is denoted by $\mathbf{x}$.

a simpler model of the direct problem is used: $\mathbf{q}$ are plane wave amplitudes. Then: $G_{ml} = e^{j\mathbf{k}_l\cdot\mathbf{x}_m}$ with $\mathbf{k}_l$ being the wavenumber vector for the l-th plane wave. We adhere to the $e^{-j\omega t}$ time convention. The direct problem includes L sources and M pressure sensors, hence explaining the matrix and vectors dimensions reported in Eq. (2).

The goal of inverse problem is to predict the measured sound field at the microphone array: $\mathbf{p} \approx \hat{\mathbf{p}}$ using a known system model $\mathbf{G}$. A typical approach to that problem is to cast it as a minimization problem with Tikhonov regularization [13]

$$\mathbf{q}_\lambda = \operatorname{argmin}\left\{||\hat{\mathbf{p}} - \mathbf{G}\mathbf{q}||_2^2 + \lambda^2\Omega(\mathbf{q})^2\right\}. \tag{3}$$

Accordingly, the quadratic sum of the prediction error $\mathbf{e} = \hat{\mathbf{p}} - \mathbf{p}$ at the microphone array is attenuated. The inverse problem solution $\mathbf{q}_\lambda$ should approach the real sound source distribution or should, at least, be able to achieve SFE. The fact that the discrete direct model $\mathbf{G}$ is representative of acoustical wave propagation suggests that if the prediction is good at the array (i.e. $\mathbf{e} \approx \mathbf{0}$), the recreated sound field in the vicinity of the array should also approach the exact measured sound field. In Eq. (3), $||\cdot||_2$ represents the vector 2-norm, λ is the penalization parameter and $\Omega(\cdot)$ is a discrete smoothing norm. For classical Tikhonov regularization, the discrete smoothing norm is the solution vector 2-norm [13]: $\Omega(\mathbf{q}) = ||\mathbf{q}||_2$. The optimal solution of Eq. (3) the becomes [8, 13, 14]

$$\mathbf{q}_\lambda = \frac{\mathbf{G}^H\hat{\mathbf{p}}}{\mathbf{G}^H\mathbf{G} + \lambda^2\mathbf{I}}. \tag{4}$$

Once the inverse problem solution $\mathbf{q}_\lambda$ is obtained from Eq. (4), the extrapolated sound pressure field [Pa] at any location $\mathbf{x}$ is then computed using a linear combination of plane waves

$$p(\mathbf{x}) = \sum_{l=1}^{L} e^{i\mathbf{k}_l\cdot\mathbf{x}}q_l, \tag{5}$$

where the complex plane wave distribution q_l is "centered" around the coordinate system origin $\mathbf{x} = \mathbf{0}$. Indeed, one notes that the sound pressure at the origin is the direct linear combination of the plane wave complex amplitudes

$$p(\mathbf{0}) = \sum_{l=1}^{L} q_l. \tag{6}$$

However, one should keep in mind that a plane wave source model could be replaced with any source model. Therefore, the selection of the plane wave sources does not limit the generality of this method.

For any field point $\bar{\mathbf{x}}$ that excludes the array origin, it would be interesting to obtain an expression similar to Eq. (6) where a new complex plane wave distribution $\bar{\mathbf{q}}$ would be centered around the field point $\bar{\mathbf{x}}$. This is expressed as follows

$$p(\bar{\mathbf{x}}) = \sum_{l=1}^{L} \bar{q}_l(\bar{\mathbf{x}}), \tag{7}$$

with

$$\bar{q}_l(\bar{\mathbf{x}}) = e^{j\mathbf{k}_l \cdot \bar{\mathbf{x}}} q_l. \tag{8}$$

This simple expression will allow the direct computation of Ambisonics signals in $\bar{\mathbf{x}}$ from $\bar{\mathbf{q}}$. According to Eq. (5), it is now assumed that the inverse problem solution q_l is a plane wave description of the measured sound field. It will now be refereed as the full-spherical plane wave description of the sound field. This operation somewhat corresponds to a three-dimensional spatial Fourier (or plane wave) transform [6] to obtain an angular spectrum. However, it was achieved here without any assumption about the array geometry. Spatial Fourier transform methods are more constraining: they need a regular microphone array geometry that fits the spatial transform coordinates system [6].

2.2. Review of beamforming

It is possible to write the simple delay-and-sum beamforming spatial responses $\mathbf{Q}_{\mathrm{BF}} \in \mathbb{C}^L$ using [15]

$$\mathbf{Q}_{\mathrm{BF}} = \mathbf{G}^H \hat{\mathbf{p}}, \tag{9}$$

or for the l-th listening direction (or point)

$$Q_{\mathrm{BF}_l} = \mathbf{g}_l^H \hat{\mathbf{p}}, \tag{10}$$

where the columns $\mathbf{g}_l$ of matrix $\mathbf{G}$ (as in Eq. (1)) exactly corresponds to a classical non-normalized steering vector used for non-focused (plane waves) beamforming (it is also possible to use focused beamforming if point sources were used in the initial direct problem Eq. (1)). Indeed, the steering vector is the evaluation of the Green function for one listening direction (or point) at the microphone array. This corresponds to the $\mathbf{G}$ definition.

2.3. Inverse problem: beamforming regularization

In our recent theoretical work [3], we finally reached the conclusion that inverse problem sensitivity to measurement noise is best controlled using Tikhonov-like regularization method. To obtain an even better spatial resolution, we investigated the possibility to use a "beamforming regularization matrix" $\mathbf{L}$ in the discrete smoothing norm: $\Omega_{\mathrm{BF}}(\mathbf{q}) = ||\mathbf{L}\mathbf{q}||_2$. The original idea was to take into account *a priori* information obtained by delay-and-sum beamforming to wisely regularize the inverse problem. The diagonal matrix $\mathbf{L}$ is given by

$$\mathbf{L} = \left[\mathrm{diag}\left(|\mathbf{G}^H \hat{\mathbf{p}}| / ||\mathbf{G}^H \hat{\mathbf{p}}||_\infty\right)\right]^{-1} \in \mathbb{R}^{L \times L}. \tag{11}$$

where $|\cdot|$ denotes elementwise absolute value of the argument and $||\cdot||_\infty$ is the vector infinite norm [16]. As one can note, the effect of $\mathbf{L}$ is to put a stronger penalization on the sources in $\mathbf{q}$ for which the delay-and-sum beamforming gives a low output. Solution of the minimization problem Eq. (3) is

$$\mathbf{q}_{\mathrm{BF}_\lambda} = \frac{\mathbf{G}^H \hat{\mathbf{p}}}{\mathbf{G}^H \mathbf{G} + \lambda^2 \mathbf{L}^H \mathbf{L}}, \tag{12}$$

or

$$\mathbf{q}_{\mathrm{BF}_\lambda} = \frac{\mathbf{G}^H \hat{\mathbf{p}}}{\mathbf{G}^H \mathbf{G} + \lambda^2 \left[\mathrm{diag}\left(|\mathbf{Q}_{\mathrm{BF}}| / ||\mathbf{Q}_{\mathrm{BF}}||_\infty\right)^2\right]^{-1}}, \tag{13}$$

where $\mathrm{diag}(\cdot)^2$ represents the elementwise squared values of a vector placed on the main diagonal of a square matrix. Preliminary theoretical studies provided promising results. Further theoretical developments and explanations of this method is the topic of manuscript under review for the Journal of Sound and Vibration [11].

3 DERIVATION OF AMBISONICS SIGNALS FROM PLANE WAVE DESCRIPTION

In this section, the derivation of the HOA signals from the inverse problem solution ($\mathbf{q}_\lambda$ or $\mathbf{q}_{\mathrm{BF}_\lambda}$) is first presented. To illustrate the validity of the proposed derivation method, a theoretical test case is reported for the direct comparison of the exact HOA signals with the predicted HOA signals.

3.1. Theory

Within the field of spatial audio, Ambisonics is an established method both for sound field reproduction and sound field capture [17, 18]. As it will be shown in the next paragraphs, the proposed SFE method based on irregular microphone array and inverse problem formulation can easily be used to derive the Ambisonics signals from the inverse problem solution $\mathbf{q}_\lambda$ or $\mathbf{q}_{\mathrm{BF}_\lambda}$, as long as the spatial aliasing criterion is respected. Moreover, one of the great interest of Ambisonics signals derivation from SFE or inverse problem theory is that virtual HOA microphones can be placed anywhere in the effective SFE region. This cannot be done using a single sound-field microphone [17] in a given point. This possibility and corresponding nomenclature are depicted in Fig. 2. This opens onto many potential applications, including the post-processing translation of the sound field capture point that feeds the HOA decoders at the reproduction stage. This possible dependency of the HOA signals (W, X, Y, Z, R, S, T, U and V) on spatial coordinates $\mathbf{x}$ is a new view of the HOA signals. To highlight this different paradigm, the dependency of the HOA signals will always be identified as in $W(\bar{\mathbf{x}})$ where $\bar{\mathbf{x}}$ is the translated coordinate system origin as introduced in Eq. (7) and shown in Fig. 2.

One can directly derive the B-Format Ambisonics first-order signals $W(\bar{\mathbf{x}})$, $X(\bar{\mathbf{x}})$, $Y(\bar{\mathbf{x}})$ and $Z(\bar{\mathbf{x}})$ from the zero and first order spherical harmonics [6] coefficients that corresponds to a plane wave distribution $\mathbf{q}$ ($\mathbf{q}_\lambda$ or $\mathbf{q}_{\mathrm{BF}_\lambda}$) [5].

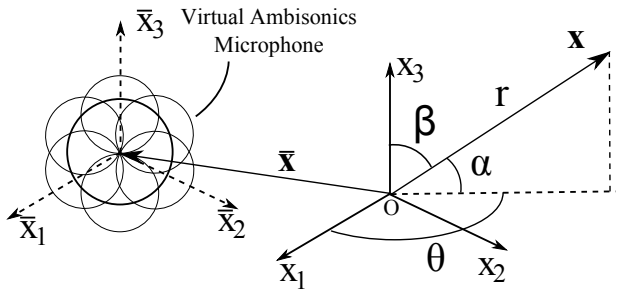

Figure 2: Schematic representation of the coordinate system and virtual Ambisonics first-order microphone in $\bar{\mathbf{x}}$.

However, in this paper, we will simply rely on the derivation of the Ambisonics B-Format from virtual microphones with appropriate directivity (Γ_W, Γ_X, etc.) in agreement with the Furse-Malham higher-order format [19]. Therefore, one writes the first-order Ambisonics signals for any field point $\bar{\mathbf{x}}$ from the translated plane wave distribution $\bar{\mathbf{q}}(\bar{\mathbf{x}}, \mathbf{q})$ (Eq. (8))

$$W(\bar{\mathbf{x}}) = \sum_{l=1}^{L} \Gamma_W(\theta_l', \alpha_l')\bar{q}_l = 1/\sqrt{2}\sum_{l=1}^{L} \bar{q}_l, \quad (14)$$

$$X(\bar{\mathbf{x}}) = \sum_{l=1}^{L} \Gamma_X(\theta_l', \alpha_l')\bar{q}_l = \sum_{l=1}^{L} \cos(\theta_l')\cos(\alpha_l')\bar{q}_l, \quad (15)$$

$$Y(\bar{\mathbf{x}}) = \sum_{l=1}^{L} \Gamma_Y(\theta_l', \alpha_l')\bar{q}_l = \sum_{l=1}^{L} \sin(\theta_l')\cos(\alpha_l')\bar{q}_l, \quad (16)$$

$$Z(\bar{\mathbf{x}}) = \sum_{l=1}^{L} \Gamma_Z(\theta_l', \alpha_l')\bar{q}_l = \sum_{l=1}^{L} \sin(\alpha_l')\bar{q}_l, \quad (17)$$

where the angles $\theta_l' = \theta_l + \pi$ and $\alpha_l' = -\alpha_l$ are the listening directions in $\bar{\mathbf{x}}$. They are introduced to distinguish the plane wave propagation directions θ_l, α_l from the corresponding listening directions θ_l', α_l'. In the case of full-sphere second-order Ambisonics, the $R(\bar{\mathbf{x}})$, $S(\bar{\mathbf{x}})$, $T(\bar{\mathbf{x}})$, $U(\bar{\mathbf{x}})$, and $V(\bar{\mathbf{x}})$ components are easily derived as follows

$$R(\bar{\mathbf{x}}) = \sum_{l=1}^{L} \Gamma_R(\theta_l', \alpha_l')\bar{q}_l = \sum_{l=1}^{L} (1.5\sin(\alpha_l')^2 - 0.5)\bar{q}_l \quad (18)$$

$$S(\bar{\mathbf{x}}) = \sum_{l=1}^{L} \Gamma_S(\theta_l', \alpha_l')\bar{q}_l = \sum_{l=1}^{L} \cos(\theta_l')\sin(2\alpha_l')\bar{q}_l \quad (19)$$

$$T(\bar{\mathbf{x}}) = \sum_{l=1}^{L} \Gamma_T(\theta_l', \alpha_l')\bar{q}_l = \sum_{l=1}^{L} \sin(\theta_l')\sin(2\alpha_l')\bar{q}_l \quad (20)$$

$$U(\bar{\mathbf{x}}) = \sum_{l=1}^{L} \Gamma_U(\theta_l', \alpha_l')\bar{q}_l = \sum_{l=1}^{L} \cos(2\theta_l')\cos(\alpha_l')^2\bar{q}_l \quad (21)$$

$$V(\bar{\mathbf{x}}) = \sum_{l=1}^{L} \Gamma_V(\theta_l', \alpha_l')\bar{q}_l = \sum_{l=1}^{L} \sin(2\theta_l')\cos(\alpha_l')^2\bar{q}_l \quad (22)$$

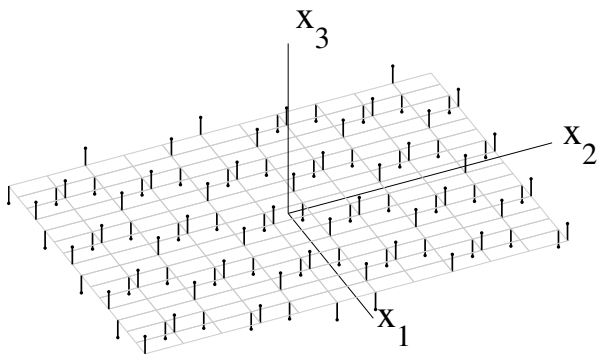

Figure 4: Microphone array geometry used for the reported theoretical and experimental results. The microphone capsules are marked by black dots. To increase the visibility of the array, vertical black lines are shown between the microphone acoustical centers and the x_1–x_2 plane. The grey lines create an horizontal grid that corresponds to the x_1, x_2 positions of the microphones.

The typical directivity patterns (Γ_W, Γ_X, etc.) associated with these Ambisonics signals are illustrated in Fig. 3 (page 5).

3.2. Verification

To verify the efficiency of the proposed HOA signals derivation from SFE and corresponding plane wave distribution as reported in Eqs. (14) to (22), a numerical simulation is proposed to compare the exact HOA signals ($\hat{W}(\bar{\mathbf{x}})$, $\hat{X}(\bar{\mathbf{x}})$, etc.) to the derived HOA signals ($W(\bar{\mathbf{x}})$, $X(\bar{\mathbf{x}})$, etc.) over an extended SFE region.

To evaluate the exact HOA signals in $\bar{\mathbf{x}}$ from numerical simulation, several assumptions are required. First, it is assumed that the HOA microphones used for that purpose are point-like with ideal directivity patterns ($\Gamma_W, \Gamma_X, \Gamma_Y$, etc.) [20]. Accordingly, the exact HOA signals are then the exact local sound pressure $\hat{p}(\bar{\mathbf{x}})$ weighted by the directivity value that correspond to exact local sound intensity opposite direction $\hat{\theta}'$, $\hat{\alpha}'$ [20]. Therefore, we write

$$\hat{W}(\bar{\mathbf{x}}) = \Gamma_W(\hat{\theta}', \hat{\alpha}')\hat{p}(\bar{\mathbf{x}}), \quad (23)$$

$$\hat{X}(\bar{\mathbf{x}}) = \Gamma_X(\hat{\theta}', \hat{\alpha}')\hat{p}(\bar{\mathbf{x}}), \quad (24)$$

$$\hat{Y}(\bar{\mathbf{x}}) = \Gamma_Y(\hat{\theta}', \hat{\alpha}')\hat{p}(\bar{\mathbf{x}}), \quad (25)$$

$$\hat{Z}(\bar{\mathbf{x}}) = \Gamma_Z(\hat{\theta}', \hat{\alpha}')\hat{p}(\bar{\mathbf{x}}), \quad (26)$$

$$\hat{R}(\bar{\mathbf{x}}) = \Gamma_R(\hat{\theta}', \hat{\alpha}')\hat{p}(\bar{\mathbf{x}}), \quad (27)$$

$$\hat{S}(\bar{\mathbf{x}}) = \Gamma_S(\hat{\theta}', \hat{\alpha}')\hat{p}(\bar{\mathbf{x}}), \quad (28)$$

$$\hat{T}(\bar{\mathbf{x}}) = \Gamma_T(\hat{\theta}', \hat{\alpha}')\hat{p}(\bar{\mathbf{x}}), \quad (29)$$

$$\hat{U}(\bar{\mathbf{x}}) = \Gamma_U(\hat{\theta}', \hat{\alpha}')\hat{p}(\bar{\mathbf{x}}), \quad (30)$$

$$\hat{V}(\bar{\mathbf{x}}) = \Gamma_V(\hat{\theta}', \hat{\alpha}')\hat{p}(\bar{\mathbf{x}}). \quad (31)$$

The verification test case involves an array of 96 microphones. The microphone array configuration is shown in

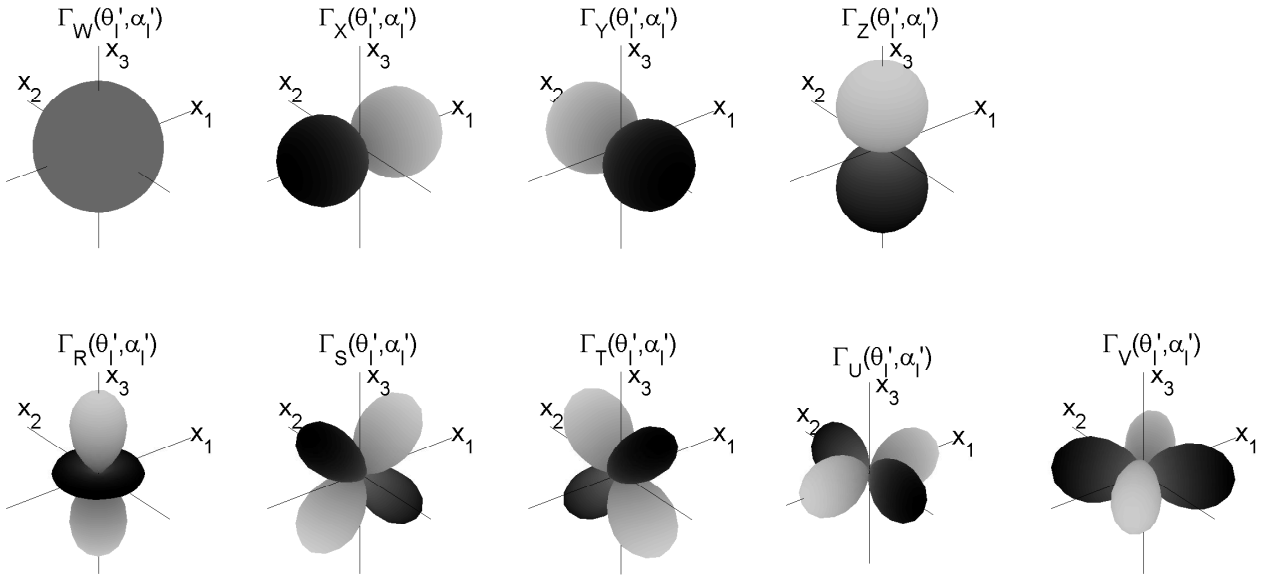

Figure 3: Second-order full-sphere Ambisonics directivity patterns according to Eqs. (14) to (22).

Fig. 4. The microphone array is arranged in a double-layer (12.25 cm vertical space) rectangular array and aligned on a horizontal grid with a spacing of 12.25 cm. The source distribution used in the direct and inverse problems is made of a spherical distribution of impinging plane waves. The direction cosines of the propagation direction of the plane wave distribution is shown in Fig. 5, 642 plane waves are used for the theoretical verification.

The true sound field and HOA signals at 600 Hz for a single monopole in $x_1 \approx -2.5$ m, $x_2 = x_3 = 0$ m in free field are shown in Fig. 14 (page 12). One can note the polarity reversal of the HOA signals as $\bar{\mathbf{x}}$ changes. This is clear in the case of $\hat{Y}(\bar{\mathbf{x}})$ shown in Fig. 14(d) where a movement along x_2 involves a polarity reversal when one crosses $x_2 = 0$. One also observes that $\hat{Z}(\bar{\mathbf{x}})$, $\hat{S}(\bar{\mathbf{x}})$ and $\hat{T}(\bar{\mathbf{x}})$ are null. This was expected since the source is located in the x_1–x_2 plane that corresponds to the illustration plane.

To achieve SFE using inverse problem theory and the beamforming regularization matrix, the inverse problem solution $\mathbf{q}_{\mathrm{BF}_\lambda}(\theta_l, \alpha_l)$ is obtained from Eq. (9) with $\lambda = 0.00001$. The inverse problem solution $\mathbf{q}_{\mathrm{BF}_\lambda}(\theta_l, \alpha_l)$ is shown in Fig. 6 (page 6). From this figure, it is clear that the SFE method based on inverse problem with the beamforming regularization matrix is able to localize the sound source from the negative x_1.

The extrapolated sound field $p(\bar{\mathbf{x}})$ and deduced HOA signals ($W(\bar{\mathbf{x}})$, $X(\bar{\mathbf{x}})$, $Y(\bar{\mathbf{x}})$, etc.) are shown in Fig. 15 (page 13). To identify the effective size of the SFE region, contour lines of the local quadratic error $e^2(\bar{\mathbf{x}})$ ($e^2(\bar{\mathbf{x}}) = |\hat{p}(\bar{\mathbf{x}}) - p(\bar{\mathbf{x}})|^2$, $e^2(\bar{\mathbf{x}}) = |\hat{W}(\bar{\mathbf{x}}) - W(\bar{\mathbf{x}})|^2$, etc.) are superimposed on the field values. Important conclusions can be drawn from this theoretical verification test case: 1) The SFE extrapolation method is able to predict the sound field in a region which is larger that the microphone array and 2) The inverse problem solution and SFE methods are able to predict the HOA signals in an effective area which is also larger that the microphone array. This validates the effectiveness of the proposed method for the derivation of HOA signals from an inverse problem approach to a measured sound field using an irregular microphone array as reported in Secs. 2 and 3.1.

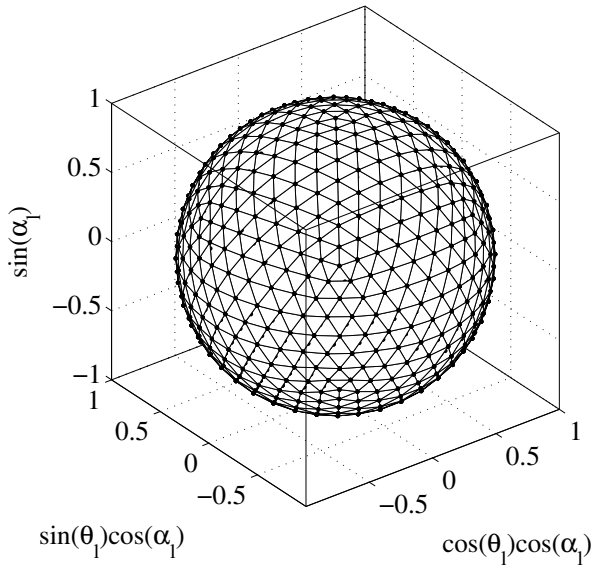

Figure 5: Direction cosines of the spherical plane wave distribution with $L = 642$ plane waves.

We recall that the effective size of the SFE area (and corresponding HOA signals predictions) are, like for classical Ambisonics using single sound-field microphone that provides first-order directivity pattern shown in Fig. 3, dependent on frequency. Larger effective extrapolation area are expected for the longer wavelengths while smaller effective SFE area are expected for smaller wavelengths. This is il-

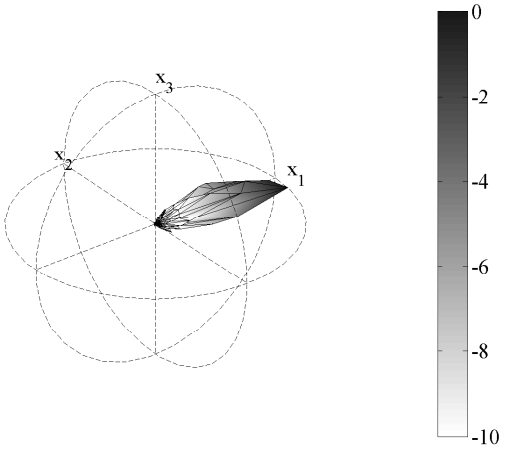

Figure 6: Absolute value (normalized to unity) of the inverse problem solution $|\mathbf{q}_{\mathrm{BF}_\lambda}(\theta_l, \alpha_l)|$ (linear (radius) and dB ref 1 (color) scales) for the verification case.

lustrated in Fig. 16 (page 14) where SFE results and local quadratic errors are reported for several frequencies for the same reported configuration. This should be kept in mind for practical applications: virtual HOA sound field capture should be done in relative close vicinity of the exact microphone array.

4 EXPERIMENTAL RESULTS

To first validate the efficiency of the proposed method for SFE and sound source localization, a sound field was measured using a microphone array in a hemi-anechoic room. The sound field was created using an omnidirectional source. The array was moved in the vicinity of the original source position and the sound field was again measured in that extrapolation region. Subsequent multichannel signal processing as presented in Sec. 2 was applied to the first measurement data to predict the sound field in the extrapolation region. To achieve the validation, we present: 1) the corresponding inverse problem solution (full-spherical plane wave description of the sound field) for comparison with the real source known position and 2) the comparison between the measured sound field in the extrapolation region and the extrapolated sound field in that region. Once this experimental validation of the SFE methods is achieved, the predicted HOA signals are presented for the experiments in Sec. 4.3.

4.1. Experimental setup

The setup is shown in Figs. 4, 7, 8(a) and 8(b) (page 7). The microphone array is made of 96 custom-made microphones arranged in a double-layer (12.25 cm vertical separation) rectangular array and aligned on a horizontal grid with a spacing of 12.25 cm. The microphones are made of electret 6 mm capsules, each microphones sensitivity is calibrated at 1 kHz. These pressure sensors are connected to eight-channel custom-made preamplifiers using high-quality analog components. These custom-built hard-

(a) Electret microphones with casing

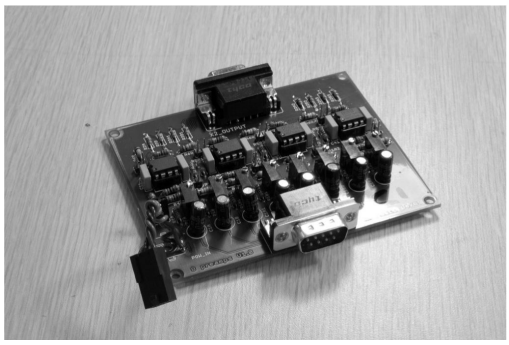

(b) 8-channel preamplifiers circuits

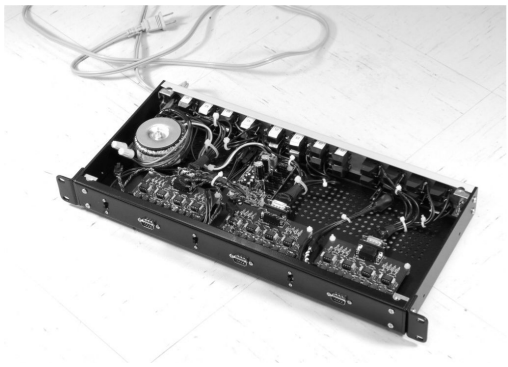

(c) 24-channel preamplifier rack

Figure 7: Pictures of the custom-built electret microphones and 24-channel preamplifier racks.

ware parts are shown in Fig. 7. They are designed for in-flight measurements of aircraft cabin sound environment evaluation and characterization. The preamplifier outputs are digitized using four MOTU$^{\mathrm{TM}}$ 24IO sound cards connected to a computer through Audiowire$^{\mathrm{TM}}$ cables. The array was installed in a hemi-anechoic chamber and the original sound field was created using a 600 Hz sinus of 1-s length on a 12-loudspeaker B&K omnidirectional source located in the plane of the antenna. The experimental setup is shown in Fig. 8(a).

4.2. Validation of the sound field extrapolation

The inverse problem solutions using classical Tikhonov regularization $\mathbf{q}_\lambda$ (Eq. (3)) or beamforming regularization matrix $\mathbf{q}_{\mathrm{BF}_\lambda}$ (Eq. (12)) are shown in Fig. 9 for the microphone array located in position b) (see Fig. 8(b)). For these two cases the regularization parameter λ was set to 1. Also note that a much denser plane wave distribution of $L = 1442$

(a) Photography of the experimental setup in the hemi-anechoic room.

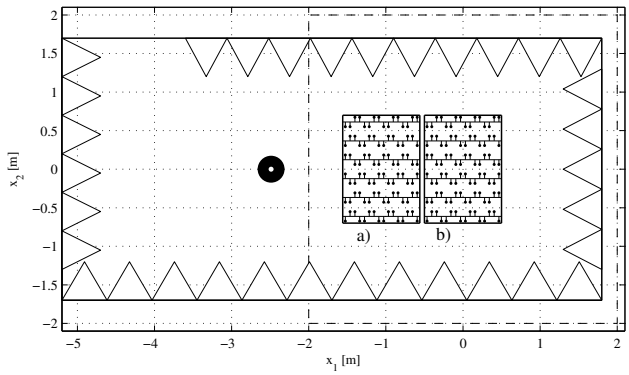

(b) Top view of the sound source and microphone array arrangement in hemi-anechoic room.

Figure 8: Photography of the experiments (a) and experimental configuration (b). The sound source is shown as a large black circle. The acoustic center of the sound source is shown as a small white dot. Two microphone array positions are labeled a) and b). For the theoretical test case, the microphone array position was b). The spatial regions that corresponds to the SFE evaluation area is circumscribed by a dash-line square.

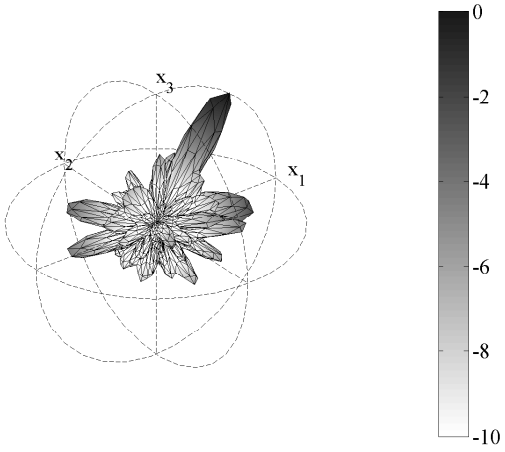

(a) Inverse problem solution $|\mathbf{q}_\lambda|$

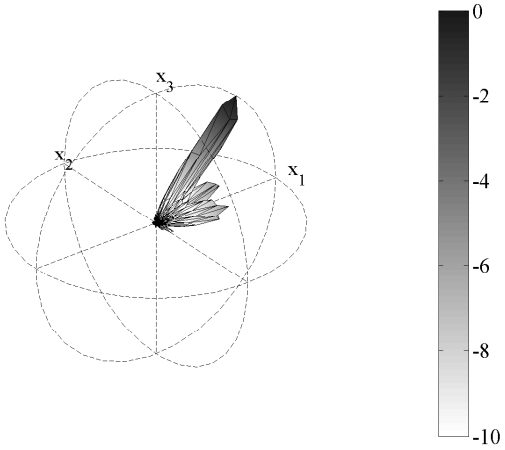

(b) Inverse problem solution $|\mathbf{q}_{\mathrm{BF}_\lambda}|$

Figure 9: Spherical mapping of the absolute value (normalized to unity) of the inverse problem solutions: (a) with classical Tikhonov regularization $|\mathbf{q}_\lambda(\theta_l, \alpha_l)|$ and (b) with beamforming regularization matrix $|\mathbf{q}_{\mathrm{BF}_\lambda}(\theta_l, \alpha_l)|$ (linear (radius) and dB ref 1 (color) scales) ($\lambda = 1$) for the experiments with the microphone array position a) (see Fig. 8(b)).

plane wave was used. Clearly, the inverse problem solution with Tikhonov regularization is not accurate: the solution is not able to localize the sound source nor the floor reflection. However, this does not mean that SFE based on classical Tikhonov regularization does not work, it only means that for this specific regularization parameter, the regularization was not strong enough. For the inverse problem solution using the beamforming regularization matrix with a similar regularization parameter λ, the solution gives something that is meaningful. Indeed, one can distinguish the direct sound source (plane waves that propagates along positive x_1) from the floor reflection (plane waves that goes upward). Therefore, this illustrates the fact that the inverse problem method using the beamforming matrix requires much less regularization to provide a meaningful result. The inverse problem solution with classical Tikhonov regularization and beamforming regularization with a stronger penalization parameter $\lambda = 25$ are shown in Fig. 10. This time, the Tikhonov solution is able to localize the sound source and the ground reflection. However, the spatial resolution is much less compared to the inverse problem with the beamforming regularization matrix shown in Fig. 9(b).

These four inverse problem solutions evaluated from a microphone array measurement in position b) (see Fig. 8(b)) were then used to predict (Eq. (5)) the sound field in array position a) (see Fig. 8(b)) for direct comparison of the SFE predictions with the true measured sound pressure field. This comparison is presented in Fig. 17 (page 15). Beside the direct comparison of the original and extrapolated sound field, the local absolute value of the prediction error is also shown. Note that the color scale used for the prediction error is not the same than for the sound fields. As expected

from the previous remarks, SFE using classical Tikhonov regularization (Figs. 17(b) and 17(c)) with $\lambda = 1$ does not provide an efficient SFE. SFE using the beamforming regularization (Fig. 17(d)) with $\lambda = 1$ does however provide a smooth extrapolation that approaches the original sound field. Moreover, one notes that for this case the prediction error is lower in the close vicinity of the measurement array (x_1 closer to 0) and higher as the extrapolation goes away from the measurement array (toward negative x_1): the extrapolation error increases as one moves away from the microphone array that provided the original measurement $\mathbf{p}(\mathbf{x}_m)$. Interestingly, SFE using classical Tikhonov regularization (Figs. 17(b) and 17(c)) with $\lambda = 25$ does provide a relatively efficient SFE. Sound field extrapolation using the beamforming regularization matrix or classical Tikhonov regularization with $\lambda = 1$ and $\lambda = 25$, respectively, are able to provide and efficient SFE, see Figs. 17(d), 17(e), 17(h) and 17(i). This illustrates a specific and advantageous feature of the beamforming regularization matrix in comparison with the classical Tikhonov regularization: the former method is much sensitive to the variation and selection of the regularization parameter. Moreover, one should keep in mind that the beamforming regularization matrix method provided the most efficient extrapolation of all the reported test cases.

To simplify the comparison of the prediction errors shown in Fig. 17, the normalized quadratic sum of the prediction error in the extrapolation area was computed: $E = 1/M \sum_{m=1}^{M} |e(\mathbf{x}_m)|^2$ [Pa^2] for each of the prediction error field $e(\mathbf{x})$ shown in Fig. 17. For the Tikhonov regularization with $\lambda = 1$, $E = 0.6446$ Pa^2. For the Tikhonov regularization with $\lambda = 25$, $E = 0.2319$ Pa^2. For the beamforming regularization approach with $\lambda = 1$, $E = 0.2070$ Pa^2 and with $\lambda = 25$, $E = 0.2194$ Pa^2. For the four test cases, the beamforming regularization approach systematically gives a lower SFE error in the extrapolation area. This validates the aforementioned feature. The general behavior of the SFE efficiency for the two methods as function of the regularization parameter λ is summarized in Fig. 11. One clearly notes that for the beamforming regularization method the prediction error goes through a larger minimum plateau: this highlights the fact that the beamforming regularization is much less sensitive to the selection of the regularization parameter λ.

4.3. Extrapolation of HOA signals

In this section, another experimental test case is reported. This time, a set of $L = 642$ plane waves as shown in Fig. 5 is used. This test case corresponds to the source and microphone array positions used for the theoretical test case. The inverse problem solution based on beamforming regularization matrix (Eq. (12)) is shown in Fig. 12 with $\lambda = 0.5$. By comparison with the theoretical test case, one notes the floor reflection that is superimposed to the direct sound.

Before actually taking a look at the extrapolated sound field and HOA signals, the comparison of the actual measurement $\hat{\mathbf{p}}$ and prediction $\mathbf{p}$ at the measuring microphone array using the inverse problem solution $\mathbf{q}_{\mathrm{BF}_\lambda}$ is shown in Fig. 13. Clearly, the predicted sound field ($\mathbf{p} = \mathbf{G}\mathbf{q}_{\mathrm{BF}_\lambda}$) approaches the measured sound field ($\hat{\mathbf{p}}$). This is supported by a low prediction error at the microphone array (Fig. 13(c)). Therefore, it is assumed that the inverse problem solution achieves its goal, i.e. ensures a prediction error close to zero $\mathbf{e} \approx \mathbf{0}$ at the measuring microphone array (see Sec. (3.1)).

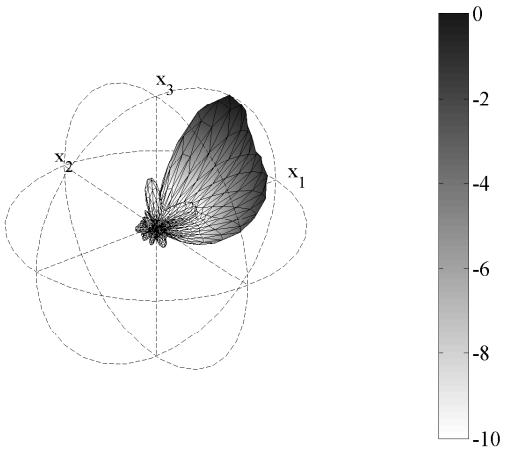

(a) Inverse problem solution $|\mathbf{q}_\lambda|$

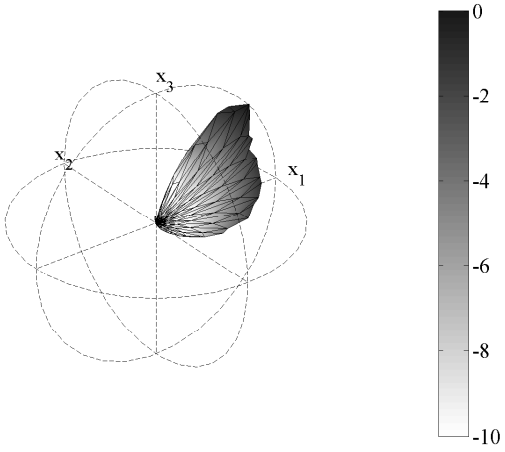

(b) Inverse problem solution $|\mathbf{q}_{\mathrm{BF}_\lambda}|$

Figure 10: Spherical mapping of the absolute value (normalized to unity) of the inverse problem solutions: (a) with classical Tikhonov regularization $|\mathbf{q}_\lambda(\theta_l, \alpha_l)|$ and (b) with beamforming regularization matrix $|\mathbf{q}_{\mathrm{BF}_\lambda}(\theta_l, \alpha_l)|$ (linear (radius) and dB ref 1 (color) scales) ($\lambda = 25$) for the experiments with the microphone array position a) (see Fig. 8(b)).

The SFE and predicted HOA signals in a SFE area that extends beyond the microphone array are presented in Fig. 18 (page 16). It is important to keep in mind that the size of the region surrounded by the walls of the anechoic space is relatively small (see Fig. 8(a)). Indeed, the SFE region shown in Fig. 18 (page 16) that covers $-2 \geq x_1 \geq 2$, $-2 \geq x_2 \geq 2$ extends somewhat beyond the surrounding boundary. Therefore, the SFE results are not expected to be

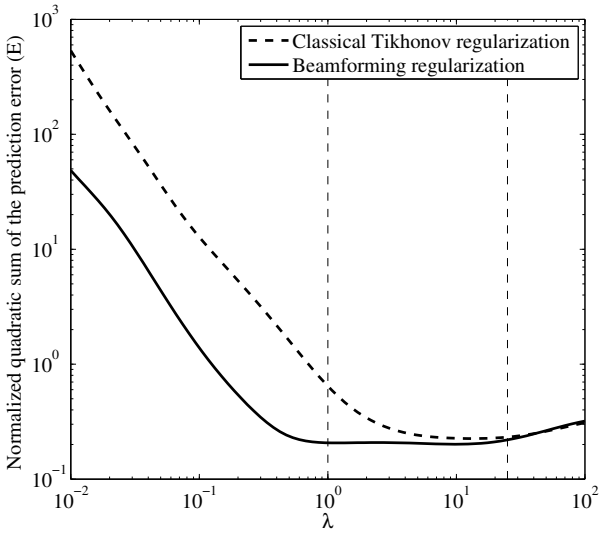

Figure 11: Normalized quadratic sum of the prediction error in the extrapolation area using classical Tikhonov regularization and beamforming regularization as function of the penalization parameter λ. The cases with $\lambda = 1$ and $\lambda = 25$ are marked by thin vertical dashed lines.

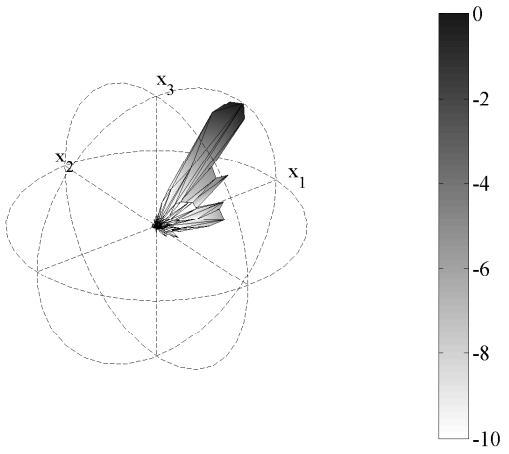

Figure 12: Absolute value (normalized to unity) of the inverse problem solution $|\mathbf{q}_{\mathrm{BF}_\lambda}(\theta_l, \alpha_l)|$ (linear (radius) and dB ref 1 (color) scales) for the experiments with the microphone array position b) (see Fig. 8(b)).

valid in that region. As expected from the equivalent theoretical test case, the strongest HOA signals are W, X, Y, R, U and V. However, by marked contrast with the theoretical test case, the concrete floor reflection introduces some significant signals for Z and S. This is expected since the ground reflection involves a propagative component along x_3. Interestingly, one notes that the Z HOA signal involves a trace wavelength in the x_1–x_2 plane that is longer than for the other HOA signals. This suggests that the Z HOA signal is able to tackle the ground reflection which involves a longer trace wavelength in the x_1–x_2 plane according to the non-null wavenumber vector component along x_3, i.e. $k_{x_3} \neq 0$ for the ground reflection. This completes the experimental prediction of HOA signals from an irregular microphone array measurement.

5 APPLICATION EXAMPLE

To facilitate the understanding and illustrate the potential of the proposed method, an application example is presented schematically in Fig. 19 (page 17). For a given sound source and sound environment (ambient sounds, room acoustics, etc.), a microphone array measurement is done and the raw data is stored. Using this raw data, virtual HOA signals are derived for any given spatial location $\bar{\mathbf{x}}$. These signals are first obtained by the transformation of the sound pressures at the microphone array in a plane wave description of the sound field using inverse problem in the frequency domain (Sec. 2). Next, the full-spherical plane wave description of the measured sound field is directly used to compute the predicted HOA signals using virtual point-like microphone with appropriate directivity patterns (Sec. 3.1). These HOA predicted signals are then converted back in the time domain to be used with any classical HOA decoder and 2D or 3D loudspeaker array.

6 CONCLUSION

The aims of this paper were twofold: provide the experimental validation of a recently proposed sound field extrapolation (SFE) method [11] and provide the derivation of higher-order Ambisonics (HOA) signals from a plane wave description of a measured sound field obtained from the SFE method.

In a first instance, the SFE method combining inverse problem theory and the beamforming regularization matrix was recalled. The obtained inverse problem solution was used to directly derive the HOA signals in an extended extrapolation area. Generally speaking, the objective of the inverse problem approach is to find a potential cause that created a measured effect. In applied acoustics, the cause is an *a priori* unknown sound source and the effect is an observed sound pressure field. To illustrate the validity of the proposed SFE method and HOA signals derivation, a simple theoretical test case was presented. It was shown that both SFE and HOA signals predictions were efficient in a extended SFE area. As for classical finite-order Ambisonics description or reproduction of a measured sound field, the effective size of the SFE region tends to get smaller for smaller wavelengths.

In a second section, we described experiments to evaluate the efficiency of the new regularization method of the inverse problem using the beamforming regularization matrix. The experiments were achieved in known and controlled conditions (an hemi-anechoic room) for validation purposes. By comparison with classical Tikhonov regularization method it was shown that this technique can offer a more precise sound source localization. Moreover, the extrapolated sound field seemed even closer to the monitored

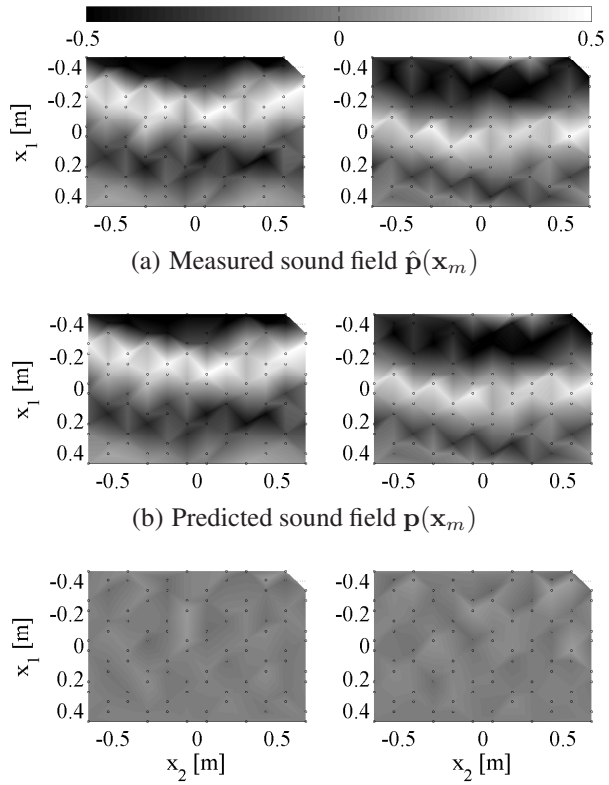

(a) Measured sound field $\hat{\mathbf{p}}(\mathbf{x}_m)$

(b) Predicted sound field $\mathbf{p}(\mathbf{x}_m)$

(c) Prediction error $\mathbf{e} = \hat{\mathbf{p}} - \mathbf{p}$

Figure 13: Real and imaginary parts (left and right, respectively) of the measurement ($\hat{\mathbf{p}}(\mathbf{x}_m)$), prediction ($\mathbf{p}(\mathbf{x}_m)$) and prediction error ($\mathbf{e} = \hat{\mathbf{p}} - \mathbf{p}$) of the experimental test case at 600 Hz at the microphone array.

sound field than for the classical regularization method. At the light of the results presented in this paper, we believe in the potential future developments, refinements, applications of the beamforming regularization method in inverse problem.

To illustrate the potential application of the HOA signals derivation for an extended region from the full-spherical plane wave description of the sound field, the HOA signals were derived from and illustrated for the experimental SFE results. Further works could be devoted to the objective and subjective comparisons of the predicted and measured HOA signals. Indeed, a direct comparison of the predicted HOA signals at a given point in space with actually measured HOA signals in that same position using a Ambisonics microphone would allow for an even more rigorous validation of the proposed HOA signals derivation.

The proposed derivation of HOA signals from a generic plane wave distribution that describes a given measured sound field opens many new possibilities for subsequent HOA reproduction. Indeed, from a single microphone array measurement, one can derive at a latter processing stage the HOA signals for any points in the SFE effective area. This is specially interesting for virtual acoustics or sound environment reproduction since it would be possible to expose a listener to an HOA reproduction of a given sound field in any points of the SFE effective area. Moreover, the proposed method is not limited to the studied microphone array configuration. Indeed, it can be applied to any microphone array geometry. This could be subject of further investigations and verifications.

Beside the evaluation of the HOA signals from the full-spherical plane wave description of the sound field (or angular spectrum [6]) obtained from the inverse problem approach, it would also be interesting to apply the derivation of HOA signals from an angular spectrum obtained from other methods such as near-field acoustical holography (NAH) that typically involves a large microphone array in close vicinity of the sound source under study. That is a virtual Ambisonics avenue that could be very interesting. Indeed, once a sound source is characterized using NAH in anechoic conditions, it would be possible to derive any HOA signals for any spatial coordinate using SFE as written in the spatial transform domain for NAH. It would then be possible to listen to the measured sound source at any relative position from the sound source. This is especially interesting for virtual acoustic applications, listening tests, sound quality and comfort studies.

7 ACKNOWLEDGMENTS

This work has been supported by CRIAQ (Consortium de Recherche et Innovation en Aérospatiale Québec), NSERC (National Sciences and Engineering Research Council of Canada) Bombardier Aerospace and CAE.

REFERENCES

[1] M.A. Poletti, "Three-dimensional surround sound systems based on spherical harmonics", Journal of the Audio Engineering Society, 53(11), 2005, 1004-1025.

[2] E. Hulsebos, D. de Vries, E. Bourdillat, "Improved Microphone Array Configurations for Auralization of Sound Fields by Wave-Field Synthesis", Journal of the Audio Engineering Society, 50(10), 2002, 779-790.

[3] P.-A. Gauthier, C. Camier, Y. Pasco, É. Chambatte, A. Berry, "Sound field extrapolation: Inverse problems, virtual microphone arrays and spatial filters", AES 40$^{\text{th}}$ International Conference, Tokyo, Japan, October 2010.

[4] C. Camier, P.-A. Gauthier, Y. Pasco, A. Berry, "Sound field reproduction applied to flight vehicles sound environments", AES 40$^{\text{th}}$ International Conference, Tokyo, Japan, October 2010.

[5] J. Daniel, R. Nicol, S. Moreau, "Further investigations of high order ambisonics and wavefield synthesis for holophonic sound imaging", Audio Engineering Society 114th Convention, Amsterdam, March 2003, Convention paper 5788.

[6] E.G. Williams, Fourier acoustics – Sound radiation and nearfield acoustical holography, Academic Press, San Diego, 1999.

[7] H. Teutsch, W. Kellermann, "Acoustic source detection and localization based on wavefield decomposi-

tion using circular microphone arrays", Journal of the Acoustical Society of America, 120(5), 2006, 2724-2736.

[8] P.A. Nelson, S.H. Yoon, "Estimation of acoustics source strength by inverse method: Part I, conditioning of the inverse problem", Journal of Sound and Vibration, 233(4), 2000, 643-668.

[9] S.H. Yoon, P.A. Nelson, "Estimation of acoustics source strength by inverse method: Part II, experimental investigation of methods for choosing regularization parameters", Journal of Sound and Vibration, 233(4), 2000, 669-705.

[10] J. Merimaa, "Applications of a 3-D microphone array", Audio Engineering Society 112^{th} Convention, Munich, May 2002, Convention paper 5501.

[11] P.-A. Gauthier, C. Camier, Y. Pasco, A. Berry, É. Chambatte, "Beamforming regularization matrix and inverse problems applied to sound field measurement and extrapolation using microphone array", under review Journal of Sound and Vibration, 2011.

[12] A.D. Pierce, Acoustics: An introduction to its physical principles and applications, Acoustical Society of America, Woddbury, 1991.

[13] C. Hansen, Rank-deficient and discrete ill-posed problems, SIAM, Philadelphia, 1998.

[14] P.A. Nelson, "A review of some inverse problems in acoustics", International journal of acoustics and vibration, 6(3), 2001, 118-134.

[15] D.N. Ward, R.A. Kennedy, R.C. Williamson, "Constant directivity beamforming", in: M. Brandstein, D. Ward (Eds.), Microphone arrays: Signal processing techniques and applications, Springer, Berlin, 2001, 3-17.

[16] G.H. Golub, C.F. van Loan, Matrix computations, John Hopkins University Press, Baltimore, 1996.

[17] F. Rumsey, Spatial audio, Focal Press, Burlington, 2001.

[18] J. Daniel, J.-B. Rault, J.-D. Polack, "Ambisonics encoding of other audio formats for multiple listening conditions", Audio Engineering Society 105^{th} Convention, San Francisco, September 1998, Convention paper 4795.

[19] A. Southern, D. Murphy, "A second order differential microphone technique for spatially encoding virtual room acoustics", Audio Engineering Society 124^{th} Convention, Amsterdam, May 2008, Convention paper 7332.

[20] H. Hacihabiboğlu, B. Günel, Z. Cvetković, "Simulation of directional microphones in digital waveguide mesh-based models of room acoustics", IEEE Transactions on Audio, Speech, and Language Processing, 18 (2010) 213-223.

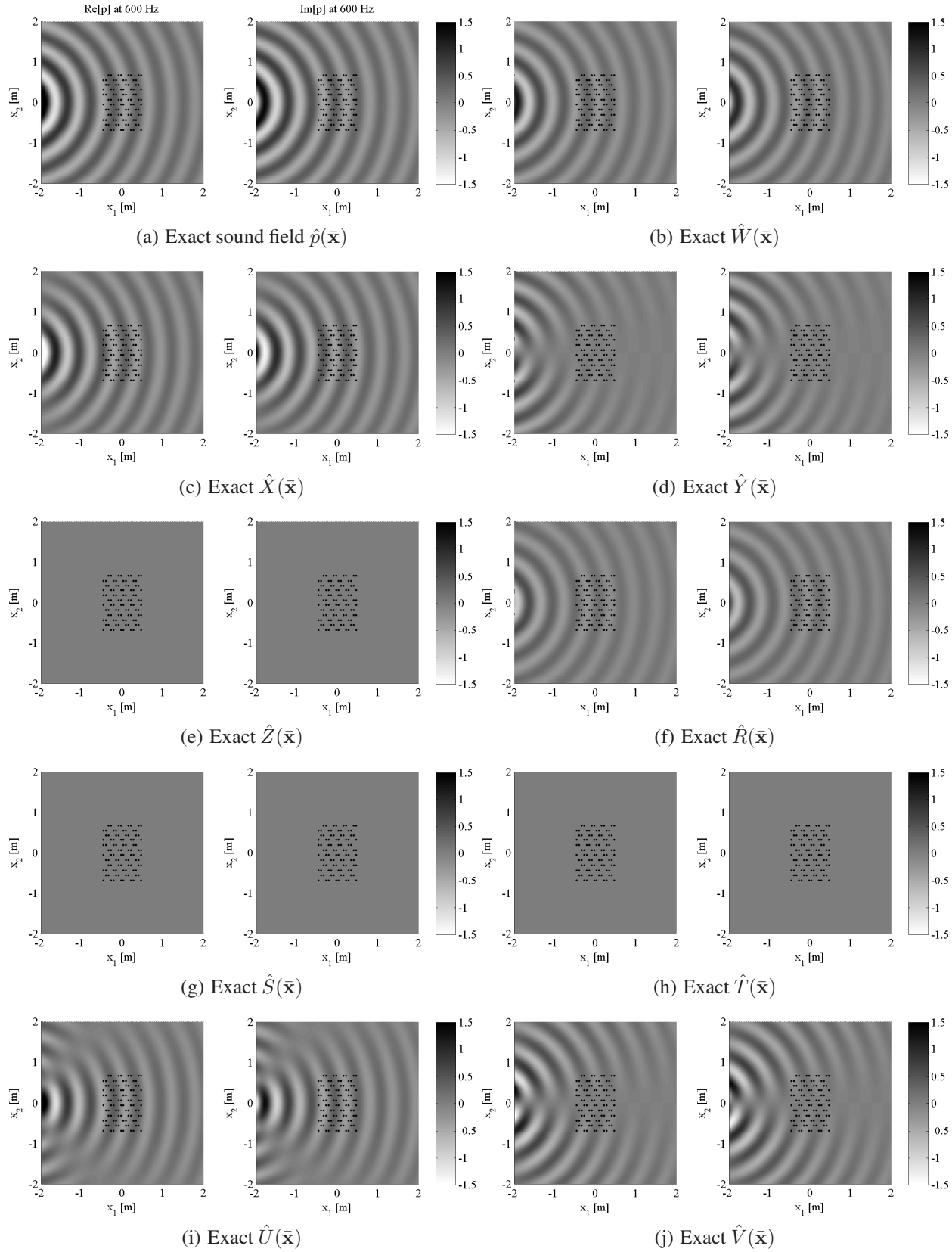

(a) Exact sound field $\hat{p}(\bar{\mathbf{x}})$

(b) Exact $\hat{W}(\bar{\mathbf{x}})$

(c) Exact $\hat{X}(\bar{\mathbf{x}})$

(d) Exact $\hat{Y}(\bar{\mathbf{x}})$

(e) Exact $\hat{Z}(\bar{\mathbf{x}})$

(f) Exact $\hat{R}(\bar{\mathbf{x}})$

(g) Exact $\hat{S}(\bar{\mathbf{x}})$

(h) Exact $\hat{T}(\bar{\mathbf{x}})$

(i) Exact $\hat{U}(\bar{\mathbf{x}})$

(j) Exact $\hat{V}(\bar{\mathbf{x}})$

Figure 14: Real and imaginary parts (left and right plots of the figures, respectively) of the exact sound pressure field $\hat{p}(\bar{\mathbf{x}})$ and Ambisonics signal fields ($\hat{W}(\bar{\mathbf{x}})$, $\hat{X}(\bar{\mathbf{x}})$, etc.) for the theoretical verification case at 600 Hz with a single monopole source in free field.

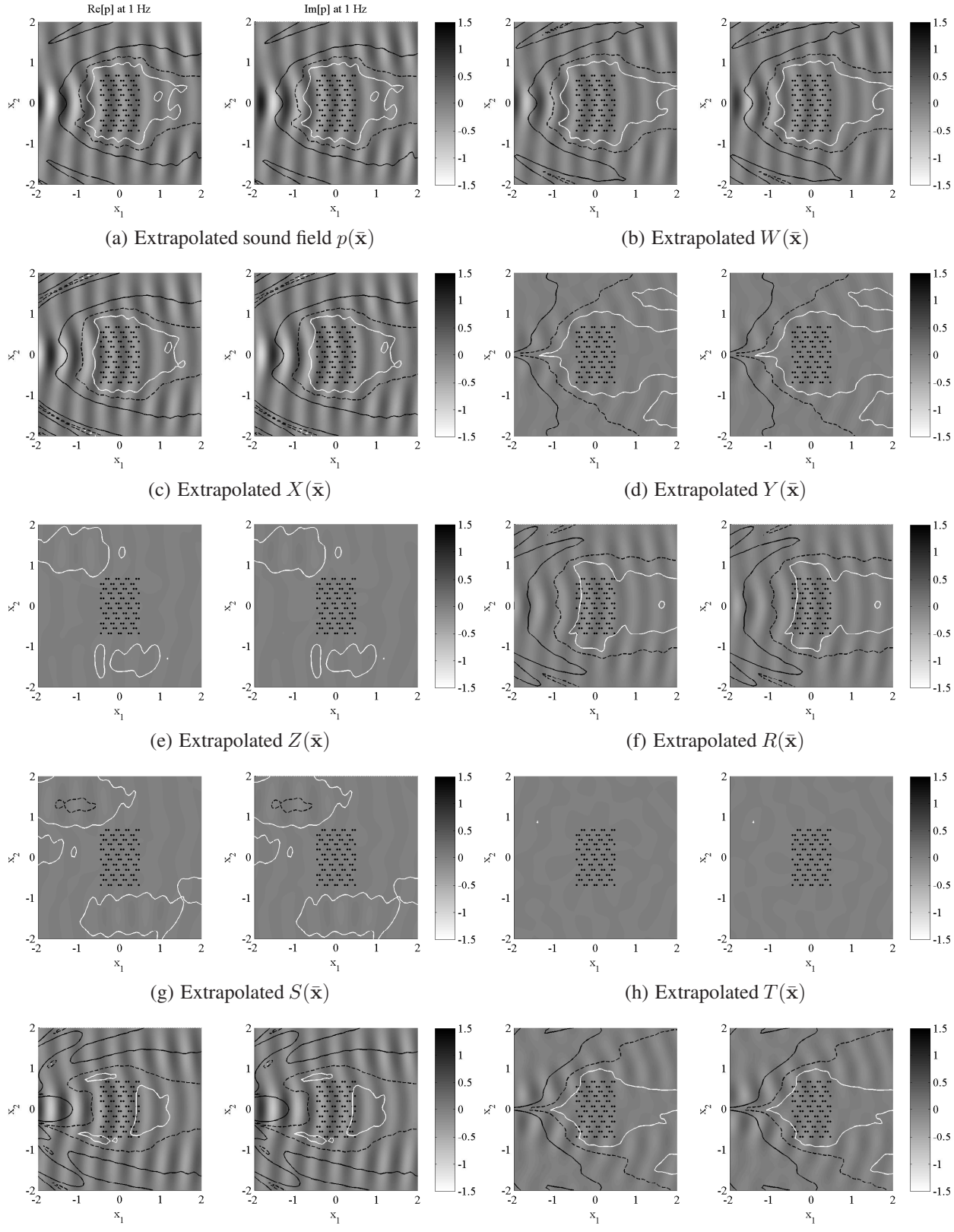

(a) Extrapolated sound field $p(\bar{\mathbf{x}})$

(b) Extrapolated $W(\bar{\mathbf{x}})$

(c) Extrapolated $X(\bar{\mathbf{x}})$

(d) Extrapolated $Y(\bar{\mathbf{x}})$

(e) Extrapolated $Z(\bar{\mathbf{x}})$

(f) Extrapolated $R(\bar{\mathbf{x}})$

(g) Extrapolated $S(\bar{\mathbf{x}})$

(h) Extrapolated $T(\bar{\mathbf{x}})$

(i) Extrapolated $U(\bar{\mathbf{x}})$

(j) Extrapolated $V(\bar{\mathbf{x}})$

Figure 15: Real and imaginary parts (left and right plots of the figures, respectively) of the extrapolated sound pressure field $p(\bar{\mathbf{x}})$ and HOA signals ($W(\bar{\mathbf{x}})$, $X(\bar{\mathbf{x}})$, etc.) for the theoretical verification case at 600 Hz with a single monopole source in free field. The local quadratic errors ($e^2(\bar{\mathbf{x}}) = |\hat{p}(\bar{\mathbf{x}}) - p(\bar{\mathbf{x}})|^2$, $e^2(\bar{\mathbf{x}}) = |\hat{W}(\bar{\mathbf{x}}) - W(\bar{\mathbf{x}})|^2$, etc.) are identified as contour lines at $e^2 = 0.001$ (white lines), $e^2 = 0.01$ (black dashed lines) and $e^2 = 0.1$ (black lines).

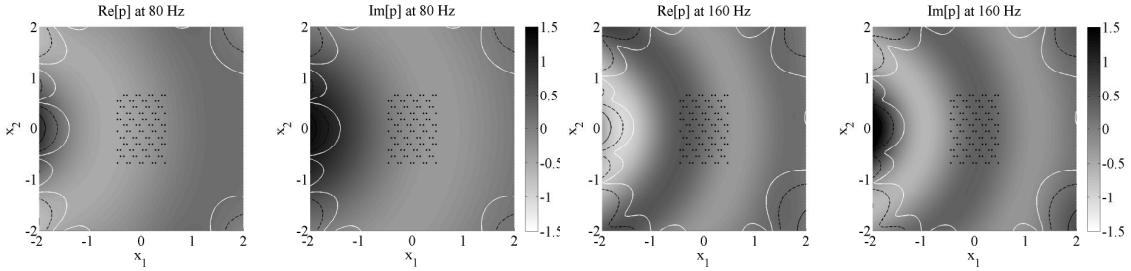

(a) Extrapolated sound field $p(\bar{\mathbf{x}})$ at 80 Hz (b) Extrapolated sound field $p(\bar{\mathbf{x}})$ at 160 Hz

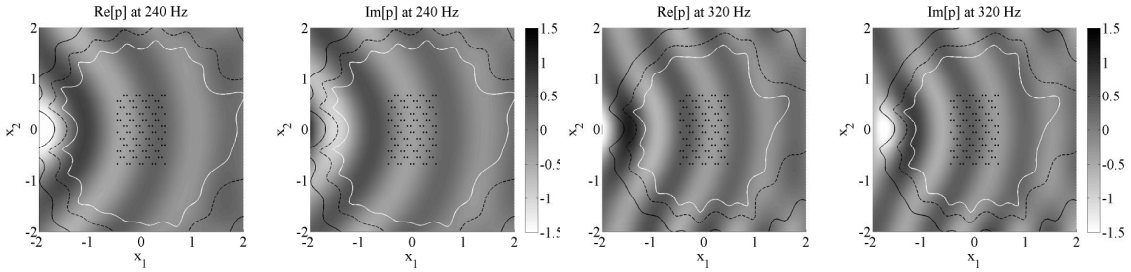

(c) Extrapolated sound field $p(\bar{\mathbf{x}})$ at 240 Hz (d) Extrapolated sound field $p(\bar{\mathbf{x}})$ at 320 Hz

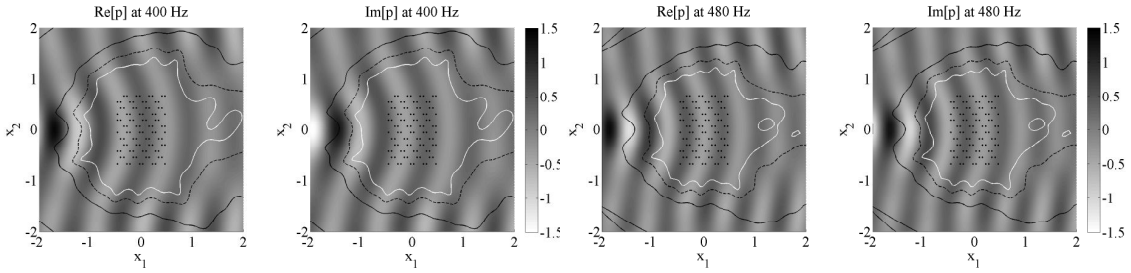

(e) Extrapolated sound field $p(\bar{\mathbf{x}})$ at 400 Hz (f) Extrapolated sound field $p(\bar{\mathbf{x}})$ at 480 Hz

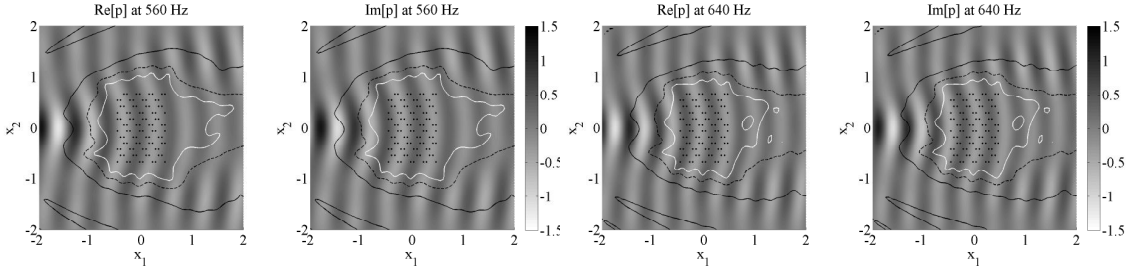

(g) Extrapolated sound field $p(\bar{\mathbf{x}})$ at 560 Hz (h) Extrapolated sound field $p(\bar{\mathbf{x}})$ at 640 Hz

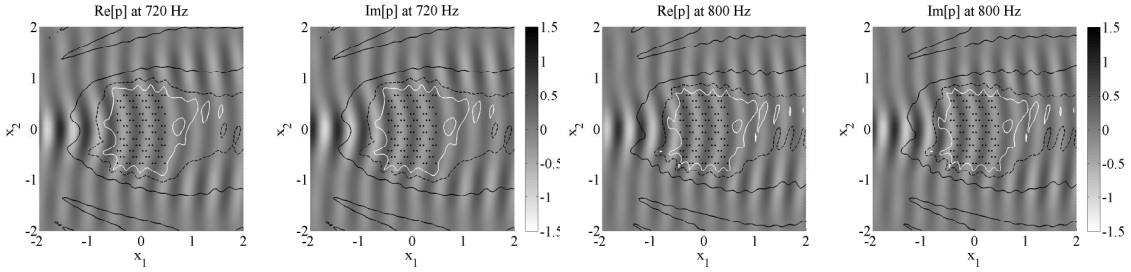

(i) Extrapolated sound field $p(\bar{\mathbf{x}})$ at 720 Hz (j) Extrapolated sound field $p(\bar{\mathbf{x}})$ at 800 Hz

Figure 16: Real and imaginary parts (left and right plots of the figures, respectively) of the extrapolated sound pressure field $p(\bar{\mathbf{x}})$ for the verification case at different frequencies with a single monopole source in free field. The local quadratic errors ($e^2(\bar{\mathbf{x}}) = |\hat{p}(\bar{\mathbf{x}}) - p(\bar{\mathbf{x}})|^2$) are identified as contour lines at $e^2 = 0.001$ (white lines), $e^2 = 0.01$ (black dashed lines) and $e^2 = 0.1$ (black lines).

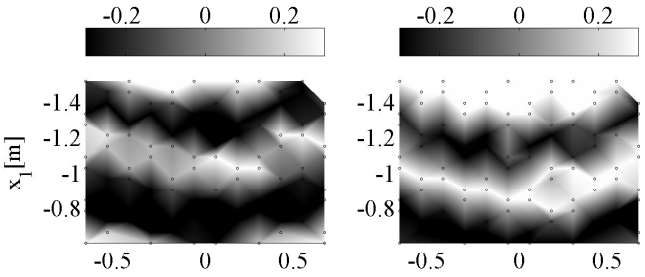

(a) Measured sound field at the monitoring array $\hat{p}(\mathbf{x})$

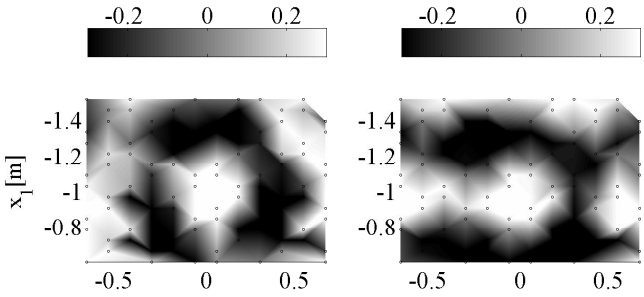

(b) Extrapolated sound field $p(\mathbf{x})$ (Tikhonov reg., $\lambda = 1$)

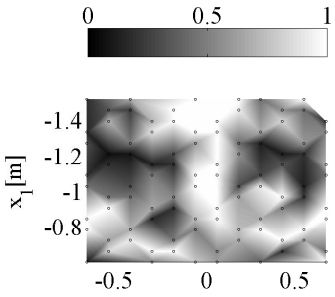

(c) Prediction error $|e(\mathbf{x})| = |\hat{p}(\mathbf{x}) - p(\mathbf{x})|$ (Tikhonov reg., $\lambda = 1$)

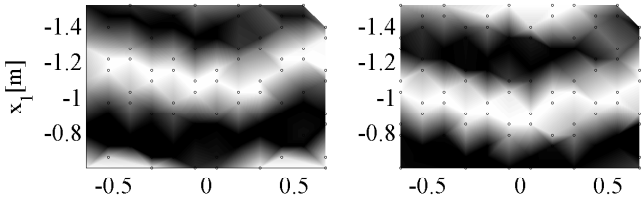

(d) Extrapolated sound field $p(\mathbf{x})$ (Beamforming reg. matrix, $\lambda = 1$)

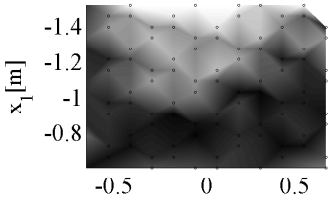

(e) Prediction error $|e(\mathbf{x})| = |\hat{p}(\mathbf{x}) - p(\mathbf{x})|$ (Beamforming reg. matrix, $\lambda = 1$)

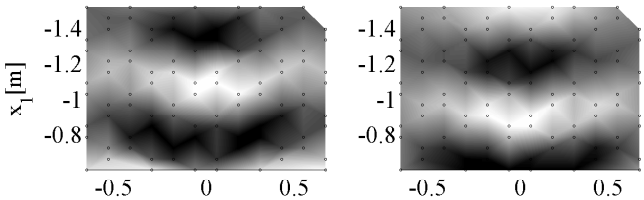

(f) Extrapolated sound field $p(\mathbf{x})$ (Tikhonov reg., $\lambda = 25$)

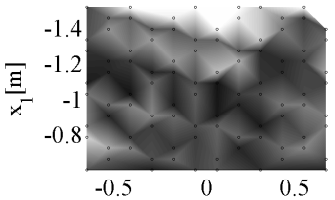

(g) Prediction error $|e(\mathbf{x})| = |\hat{p}(\mathbf{x}) - p(\mathbf{x})|$ (Tikhonov reg., $\lambda = 25$)

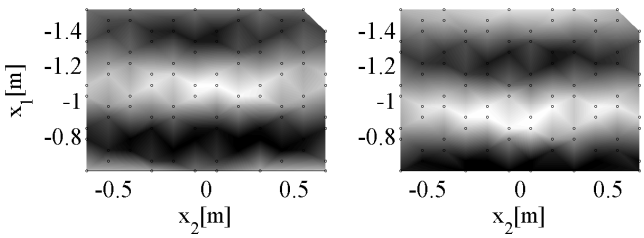

(h) Extrapolated sound field $p(\mathbf{x})$ (Beamforming reg. matrix, $\lambda = 25$)

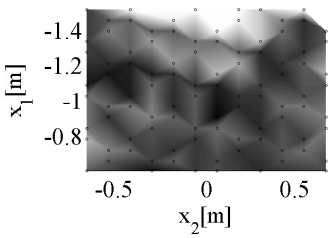

(i) Prediction error $|e(\mathbf{x})| = |\hat{p}(\mathbf{x}) - p(\mathbf{x})|$ (Beamforming reg. matrix, $\lambda = 25$)

Figure 17: Real and imaginary parts (left and right columns of (a), (b), (d), (f) and (h)) of the measured sound field $\hat{p}(\mathbf{x})$, extrapolated sound field $p(\mathbf{x})$ and absolute value of the prediction error $|e(\mathbf{x})| = |\hat{p}(\mathbf{x}) - p(\mathbf{x})|$ at the monitoring array (in an extrapolation area different from the measurement area) for different inverse problem solutions for the experiments in hemi-anechoic chamber at 600 Hz. The measurement points are shown as black circles. The color scale is different for the prediction error.

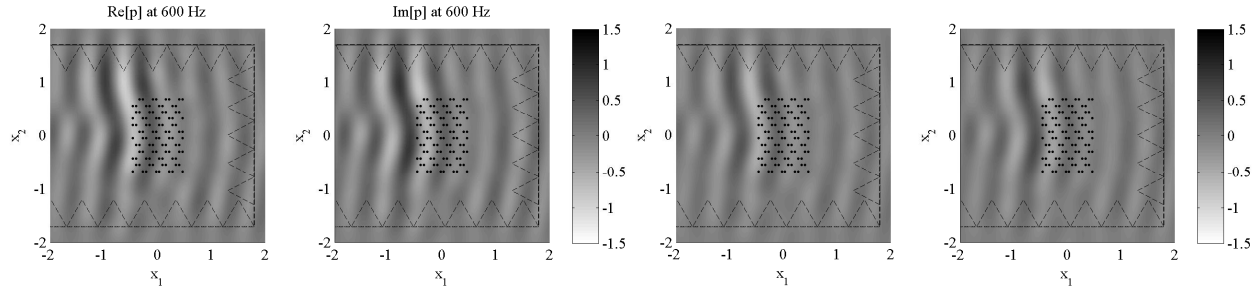

(a) Extrapolated sound field $p(\bar{\mathbf{x}})$

(b) Extrapolated $W(\bar{\mathbf{x}})$

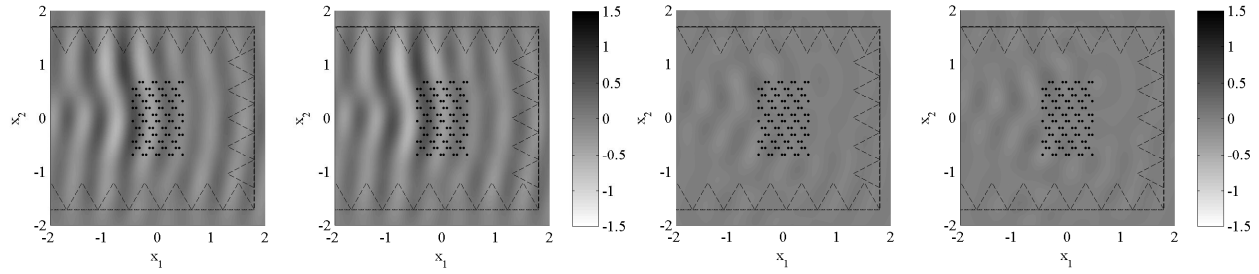

(c) Extrapolated $X(\bar{\mathbf{x}})$

(d) Extrapolated $Y(\bar{\mathbf{x}})$

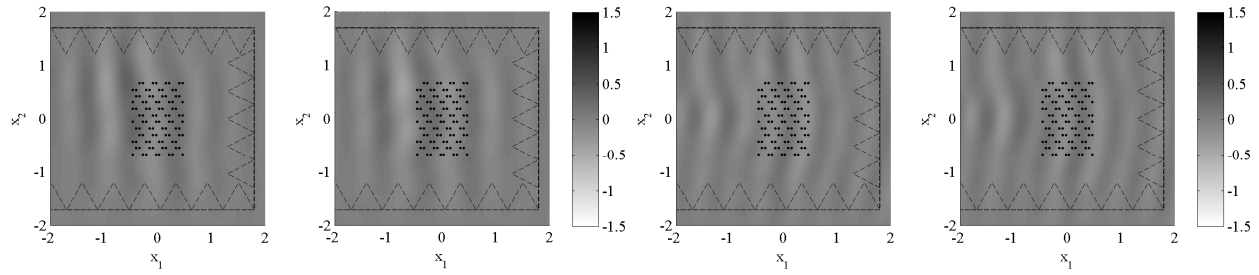

(e) Extrapolated $Z(\bar{\mathbf{x}})$

(f) Extrapolated $R(\bar{\mathbf{x}})$

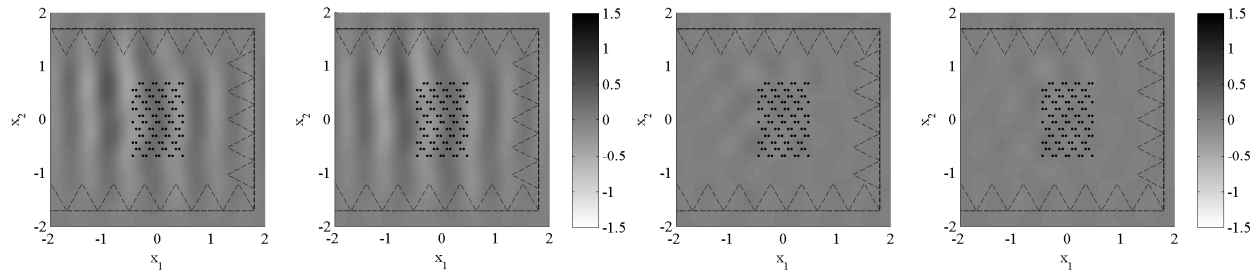

(g) Extrapolated $S(\bar{\mathbf{x}})$

(h) Extrapolated $T(\bar{\mathbf{x}})$

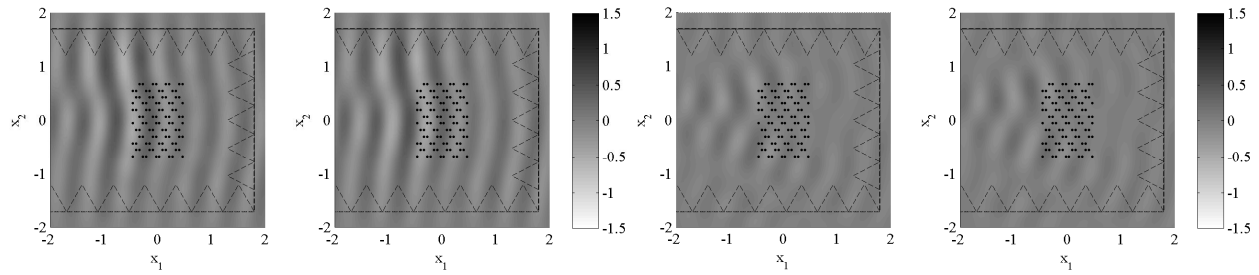

(i) Extrapolated $U(\bar{\mathbf{x}})$

(j) Extrapolated $V(\bar{\mathbf{x}})$

Figure 18: Real and imaginary parts (left and right plots of the figures, respectively) of the extrapolated sound pressure field $p(\bar{\mathbf{x}})$ and HOA signals ($W(\bar{\mathbf{x}})$, $X(\bar{\mathbf{x}})$, etc.) for the experimental case at 600 Hz. Approximate room boundary are shown as dashed black lines.

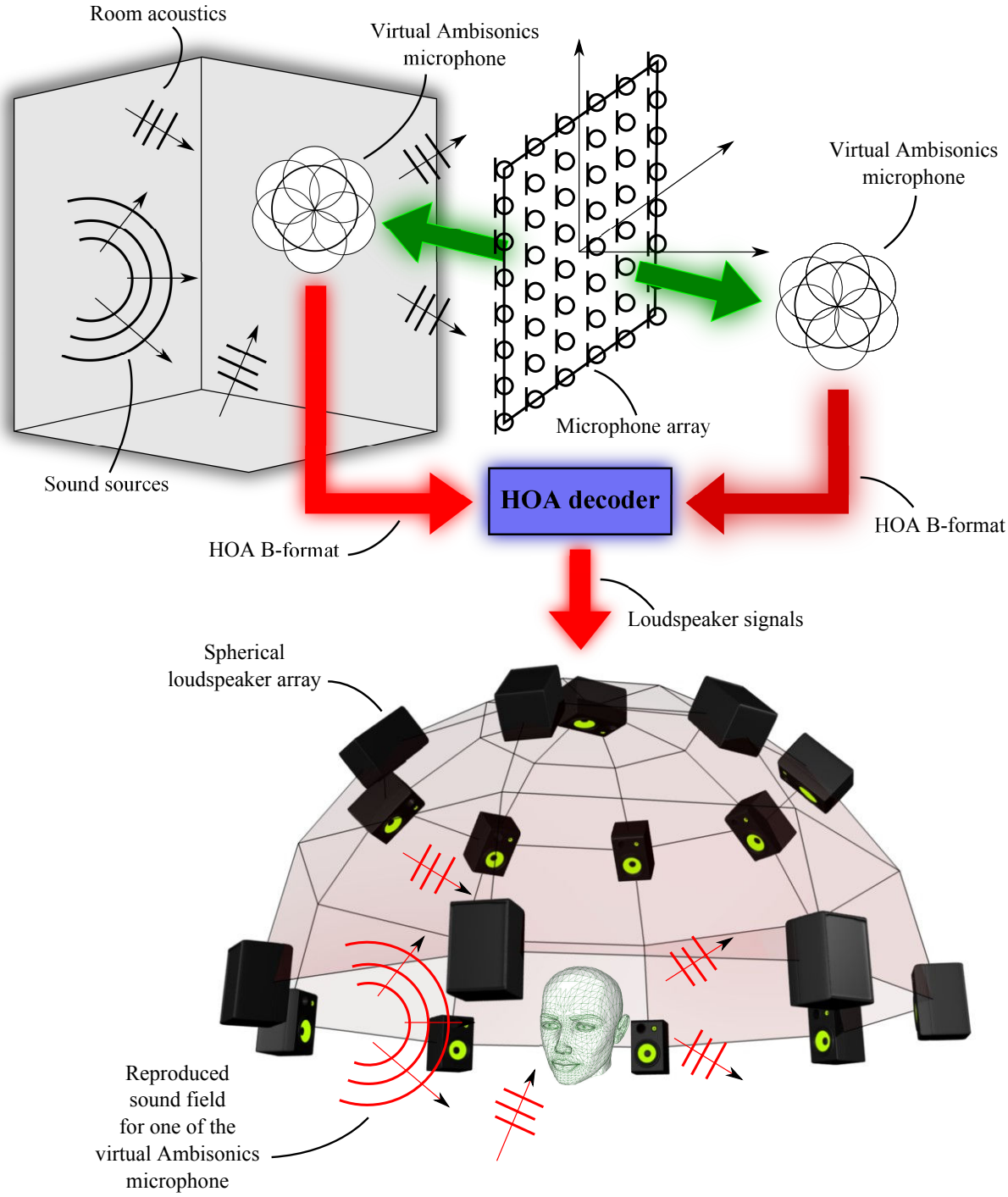

Figure 19: Illustrated application of the proposed method for two virtual Ambisonics microphones signals deduced from a single microphone array. Once the microphone array data is stored, it is possible to predict the HOA signals for any position located in the effective SFE area. These predicted HOA signals are then sent to a conventional HOA decoder and loudspeaker array for subsequent sound field reconstruction at the center of the array where the listener stands.